ACS NANO

Open Access

www.acsnano.org

Article

Negative Schottky Barriers and Spin-Polarized Fermi Crossings at $WSe_2/NbSe_2$ Interfaces

Oliver J. Clark,* Anugrah Azhar, Thi-Hai-Yen Vu, Benjamin A. Chambers, Federico Mazzola, Sadhana Sridhar, Geetha Balakrishnan, Aaron Bostwick, Chris Jozwiak, Eli Rotenberg, Sarah L. Harmer, Mohammad Saeed Bahramy, Michael S. Fuhrer, and Mark T. Edmonds

Cite This: *ACS Nano* 2026, 20, 7898–7907

Read Online

ACCESS | Metrics & More | Article Recommendations | Supporting Information

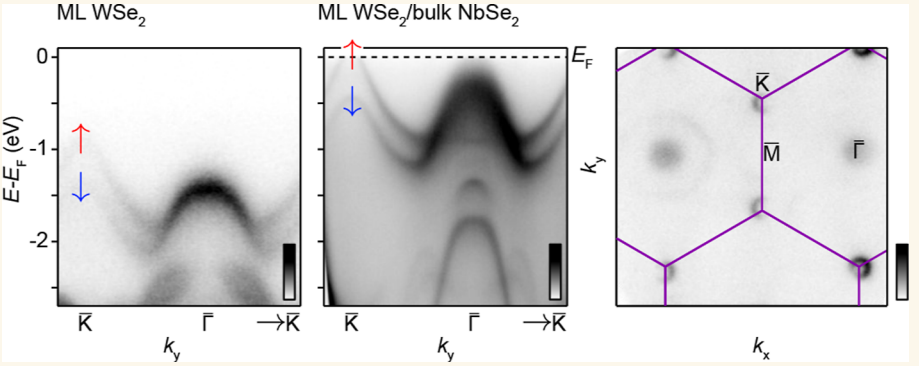

ABSTRACT: Discovering and engineering spin-polarized surface states in the electronic structures of condensed matter systems is a crucial first step in the development of spintronic devices, wherein spin-polarized bands crossing the Fermi level can facilitate information transfer. Here, through nanofocused angle-resolved photoemission spectroscopy (nano-ARPES) and density functional theory-based calculations, we show that the interface between monolayer WSe_2 and metallic $NbSe_2$ exhibits a negative Schottky barrier height of ∼ −30 meV: the K-point valleys of the semiconducting layer are shifted by ∼800 meV to produce a surface-localized Fermi surface populated only by spin-polarized charge carriers. By increasing the WSe_2 thickness, the Fermi pockets can be moved from K to Γ, demonstrating tunability of novel semimetallic phases that exist atop a substrate additionally possessing charge density wave and superconducting phases. Together, this study provides a spectroscopic understanding into p-type, Schottky barrier-free interfaces, which are of urgent interest for bypassing the limitations of current-generation vertical field effect transistors, in addition to longer-term spintronics development.

KEYWORDS: *2D material heterostructures, 2D material interfaces, p-type contacts, transition metal dichalcogenides, density functional theory, angle-resolved photoemission spectroscopy*

As the limitations of conventional electronics are reached, the semiconducting subsets of 2H-structured transition metal dichalcogenides (TMDs) have emerged as key components for ultraoptimized nanoscale electronics due to the ease with which their monolayer forms can be isolated without "dangling" bonds or residual polar charge. This facilitates, for example, the fabrication of vertical field effect transistors (VFETs) on the smallest possible length scales through interfacing with metallic 2D materials, like graphene.[1−4] Despite this promise, most pairings of semiconducting TMDs with metals are found to exhibit large Schottky barriers, rendering them unsuited for applications due to suboptimal efficiency.[1] Recent transport studies have identified $WSe_2/NbSe_2$ interfaces as a rare exception: the van der Waals nature of both materials precludes interface states from pinning the Fermi level to the band gap of the semiconductor, and the difference in work functions is compatible with the energetics of the WSe_2 valence band maxima (VBM), together facilitating an ohmic contact.[2,3] While these transport studies therefore demonstrate enormous potential for $WSe_2/NbSe_2$ systems, they do not rule out the presence of a small positive Schottky barrier at the interface. Furthermore, spectroscopic understanding of the momentum-resolved electronic structures at these interfaces is entirely lacking.

Received: December 16, 2025
Revised: February 13, 2026
Accepted: February 13, 2026
Published: February 25, 2026

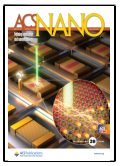

https://doi.org/10.1021/acsnano.5c22009
ACS Nano 2026, 20, 7898–7907

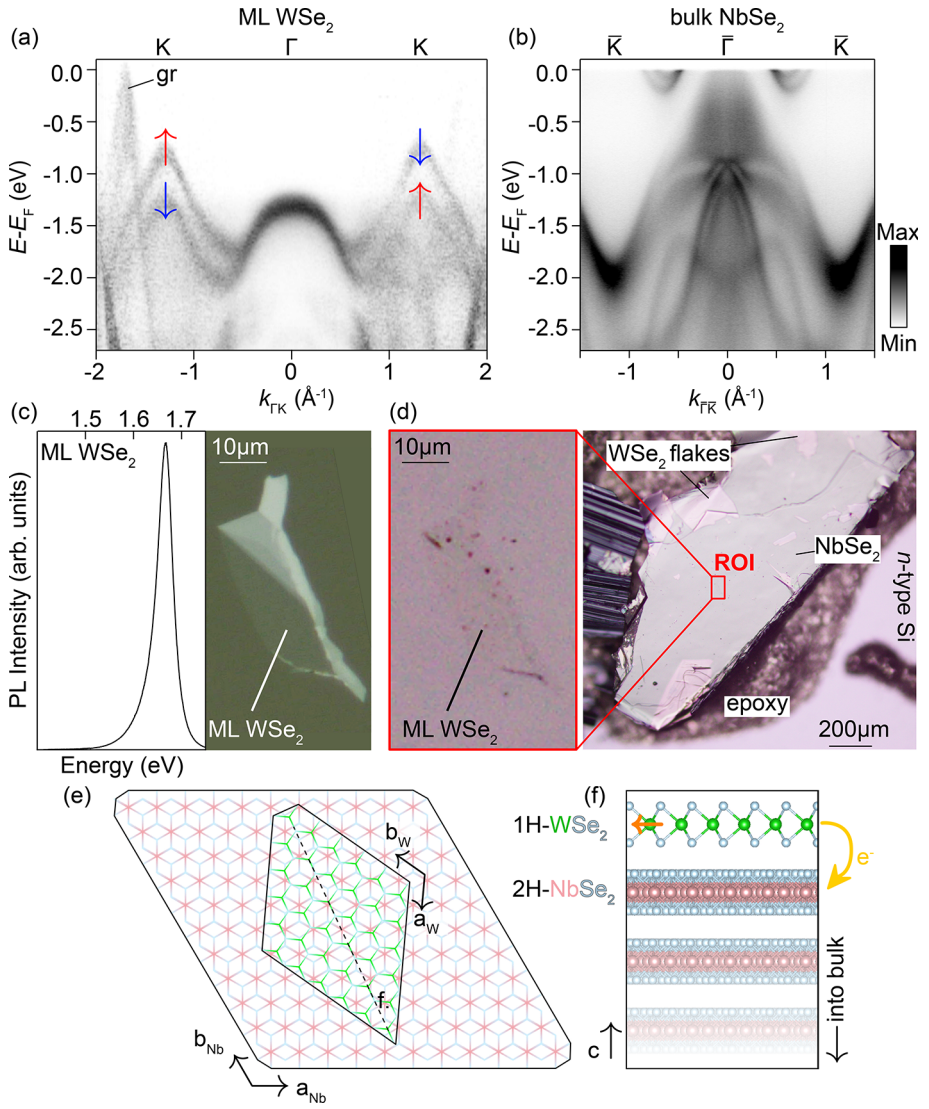

Figure 1. Electronic structures of ML WSe_2 and bulk $NbSe_2$, and heterostructure fabrication: (a) K′−Γ−K−band dispersion ($h\nu$ = 21.2 eV, T = 300 K) of a monolayer of WSe_2 deposited on a graphite/n-type Si substrate acquired with nano-ESCA. The out-of-plane spin polarization of the pair of spin−orbit split bands at K is shown, as determined in earlier works.[8] The band labeled gr originates from the graphite Dirac cone of the substrate. (b) $\overline{K'}$−$\bar{\Gamma}$−$\bar{K}$ band dispersions ($h\nu$ = 121 eV, T ∼10 K) of bulk 2H−$NbSe_2$. (c) Optical image of the flake containing the ML-WSe_2 region before transferring onto bulk $NbSe_2$ (right) and photoluminescence (PL) signal from the monolayer region of the flake (left). (d) Optical image of a $WSe_2/(NbSe_2)_n$ sample. The red box indicates the area where the WSe_2 monolayer was transferred, shown left. (e,f) Schematic diagram of a monolayer of 2H−WSe_2 placed upon bulk 2H−$NbSe_2$ with a large twist angle. $(a,b)_{W,Nb}$ are the crystallographic directions for WSe_2 (W) or $NbSe_2$ (Nb). The dashed line in the a-b plane in (e) indicates the cross section shown in (f). The orange arrow in the WSe_2 layer indicates the electric dipole giving rise to the Zeeman-like out-of-plane spin polarization indicated in (a). The yellow curved arrow shows the direction of charge transfer in this hybrid system.

Here, through nano focused angle-resolved photoemission spectroscopy (nano-ARPES) and first-principles calculations, we examine the electronic structure at the interface between monolayer WSe_2 and bulk $NbSe_2$. We not only find a negative Schottky barrier but also the formation of a rich top layer-localized Fermiology exclusively composed of spin-polarized charge carriers. We further show how these Fermi surfaces can be tuned, both in terms of spin degeneracy and positioning in momentum space, and demonstrate how the key physics of these hybrid systems is robust against lattice mismatch, thus simplifying the assembly of these functional systems.

Together, this study provides a microscopic electronic structure perspective of p-type $WSe_2/NbSe_2$ interfaces while indicating potential ways to harness the unique spin-valley locked electronic structures of semiconducting 2H-TMDs at equilibrium.

RESULTS AND DISCUSSION

Constructing $WSe_2/NbSe_2$ Interfaces

Figure 1a shows the electronic structure of monolayer WSe_2 atop a weakly interacting graphite (gr) substrate. The band structure of 2H−WSe_2, like other 2H-TMDs, naturally possesses pairs of spin−orbit split hole-like bands at the K and K′ points of its Brillouin zone (BZ). In the monolayer limit, these pairs of bands are spin-polarized out-of-plane due to an uncompensated in-plane electric dipole within a single 1H-unit[5−8] but reverse from K to K′ with time-reversal symmetry (TRS). Together, this produces oppositely polarized

https://doi.org/10.1021/acsnano.5c22009
ACS Nano 2026, 20, 7898−7907

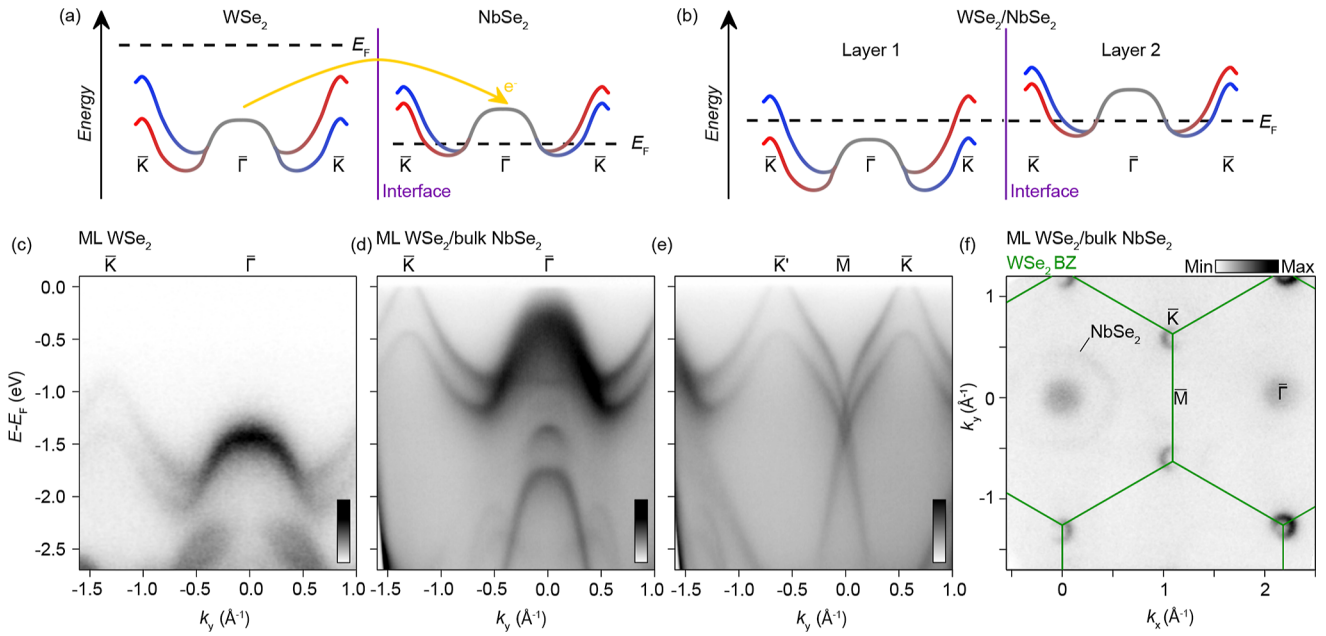

Figure 2. Fermiology of ML-WSe_2 on bulk $NbSe_2$: (a,b) Schematic diagrams of freestanding (a) and interfaced (b) WSe_2 and $NbSe_2$ systems. The band coloring indicates the out-of-plane spin polarization of the bands, though we note that for 2+ layer TMDs, the spin polarization is quenched by the adjacent layer in the unit cell. (c) Band dispersion ($h\nu$ = 114 eV) along the $\bar{K}$–$\bar{\Gamma}$–$\bar{K}$ for a free-standing WSe_2 monolayer, measured under similar experimental conditions to the heterostructure shown in (d). (d,e) Band dispersions ($h\nu$ = 91.5 eV) along the $\bar{K}$–$\bar{\Gamma}$–$\bar{K}$ (d) and $\bar{K}$–$\bar{M}$–$\bar{K}$ (e) directions of ML-WSe_2 placed on a bulk $NbSe_2$ substrate. (f) Corresponding Fermi surface ($h\nu$ = 91.5 eV). Solid lines show the BZ of WSe_2.

valence band maxima (VBM) with maximal separation in momentum space.[5−8] Electrons populating these Zeeman-like extrema at K and K′ can be selectively excited with circularly polarized light, which is directly exploited in so-called valleytronic devices.[5−7,9] However, their energetic positioning of ∼ −0.75 eV below the Fermi level prevents contributions to transport without optical pumping or gating. Unlike the global VBM at K, the local valence band maxima (lVBM) at Γ is spin degenerate for all thicknesses, though due to significant interlayer hopping capability of the W d_{z^2} orbitals from which it derives, it readily develops a large bandwidth along the k_z axis when neighboring layers are present.[10−14]

These band features are compared with those of bulk 2H−$NbSe_2$, shown in Figure 1b. The crystal and electronic structures of 2H−WSe_2 and 2H−$NbSe_2$ are qualitatively very similar. However, the Nb d^1 configuration (compared to W d^2) positions the $NbSe_2$ Fermi level below both Γ and K lVBM, creating a metallic Fermi surface with large electron and hole sheets.[15−17] The low energy band structure at $\bar{\Gamma}$ is therefore predominantly Nb d_{z^2} and Se p_z-derived and is again extremely three-dimensional due to the orbital hopping potential across the van der Waals gap, evident in photoemission spectra through the diffuse 'filled-in' spectral weight of the k_z-projected band manifold at $\bar{\Gamma}$ (Figure 1b). The electron-like sheets partway along the $\bar{\Gamma}$–$\bar{K}$ direction share the in-plane transition metal (d_{xy}, $d_{x^2-y^2}$) orbital character as the VBM of monolayer WSe_2 and therefore remain layer-locked and two-dimensional even in the many-layer limit.[17]

Figure 1c–f provides an overview of the construction and composition of the hybrid system made by pairing a monolayer WSe_2 flake to a bulk $NbSe_2$ crystal. Flakes of WSe_2 were exfoliated onto polydimethylsiloxane (PDMS) film, and the presence of monolayer regions was verified through their photoluminescence spectra (Figure 1c), which are strongly thickness-dependent for semiconducting 2H-TMDs.[18] Flakes are then transferred onto cleaved surfaces of $NbSe_2$ single crystals (Figure 1d) in an Ar glovebox. Despite the majority of the $NbSe_2$ surface remaining exposed, the monolayer WSe_2 cap is found to be sufficient to locally preserve the underlying substrate from oxidation for extended periods in atmospheric conditions. The crystal structure of the assembled WSe_2/$NbSe_2$ interface is shown in Figure 1e,f.

Spin-Polarized Fermiology of 1 ML-WSe_2/$NbSe_2$

Figure 2a,b illustrates the loss of electrons from the WSe_2 monolayer to the bulk $NbSe_2$ crystal across the interface, underpinning the transport characteristics of these p-type contacts.[2,3] The charge transfer is facilitated by the respective out-of-plane orbital-derived bands at $\bar{\Gamma}$ in both materials, which readily hybridize when the constraints of 2D quantization are lifted. In contrast to previous reports, which could not rule out small positive Schottky barriers across similar WSe_2/$NbSe_2$ interfaces,[2,3] our ARPES spectra in Figure 2c,f establish that the charge transfer from monolayer WSe_2 to the bulk $NbSe_2$ substrate is sufficient in scale to drive the formation of a semimetallic WSe_2 ground state, thus implying a perfect ohmic contact between these two materials.

Remarkably, the Fermi level is repositioned between the WSe_2 lVBM at K and Γ to produce a top-layer electronic structure with momentum-separated Fermi pockets which are likely spin-polarized (as justified below). Band dispersions along the $\bar{K}$–$\bar{\Gamma}$–$\bar{K}$ and $\bar{K}$–$\bar{M}$–$\bar{K}$ directions in Figures 2d and 2e, respectively, show the full valence band structure of this charge-doped system. In comparison to a free-standing ML-WSe_2 case (Figure 2c), while the d_{z^2}-derived lVBM at Γ is significantly broadened due to interactions with the out-of-plane orbital-derived bands of the substrate, the remainder of the electronic structure, derived from in-plane orbitals with negligible out-of-plane hopping, is relatively unchanged other than the $\Delta E \approx 0.85$ eV shift toward the Fermi level. This is calculated from the energy difference of the deeper-lying K-

https://doi.org/10.1021/acsnano.5c22009
ACS Nano 2026, 20, 7898−7907

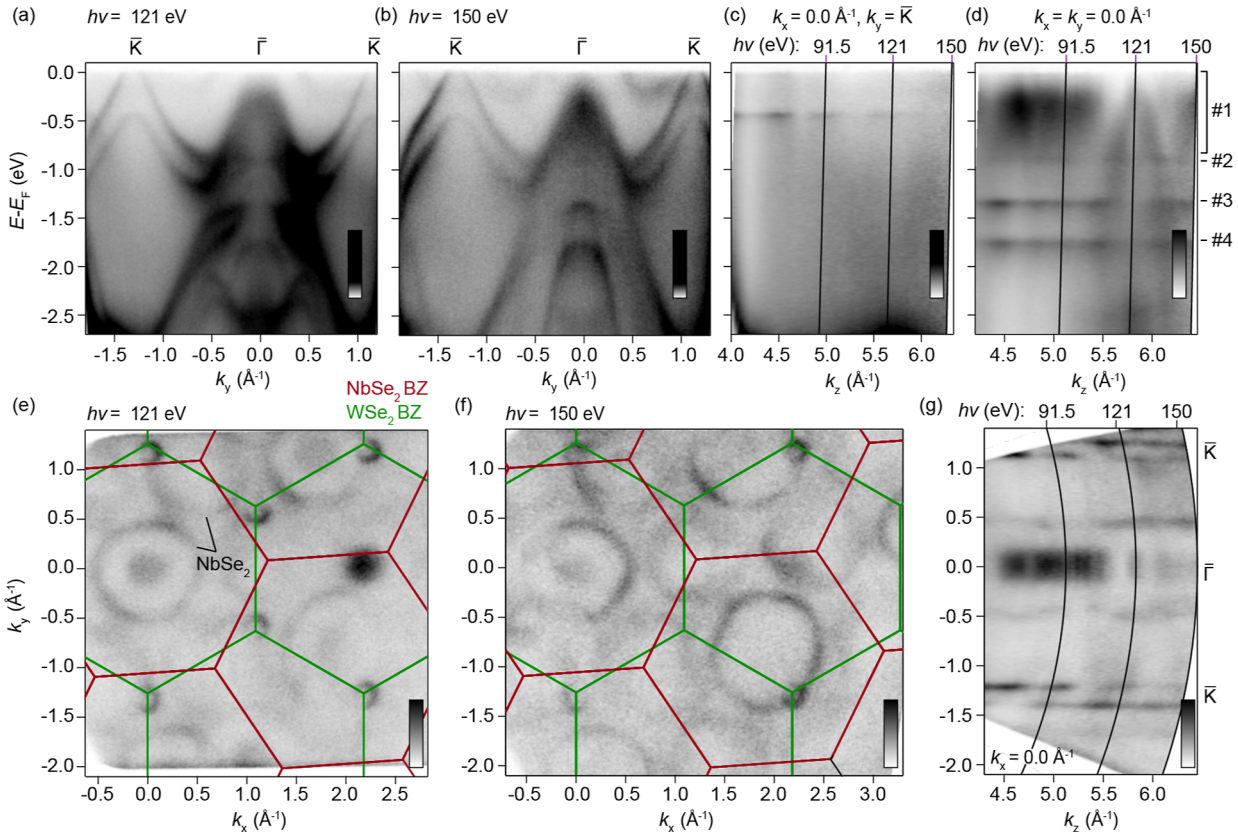

Figure 3. Mixed band dimensionality in ML-WSe_2/bulk $NbSe_2$: (a,b) Band dispersions along the $\bar{K}$–$\bar{\Gamma}$–$\bar{K}$ directions for $h\nu$ = 121 eV (a) and (b) 150 eV. (c,d) k_z dispersions through the $\bar{K}$ point (c) and $\bar{\Gamma}$ point (d) constructed by varying the incident photon energy between 60 and 150 eV (V_0 = 13 eV). (e,f) Fermi surface maps taken with $h\nu$ = 121 eV (e) and 150 eV (f). Red and green solid lines are Brillouin zone contours for $NbSe_2$ and WSe_2, respectively. (g) k_y–k_z constant energy contour at the Fermi level constructed by varying the incident photon energy between 60 and 150 eV (V_0 = 13 eV). Black lines in (c,d,g) indicate the k_z positioning of the 91.5 eV, 121 eV, and 150 eV data sets shown in Figures 2 and 3. The four distinct bands in (d) are labeled from low binding energy to high.

point valley between the data in Figures 1 and 2 and is found to be consistent across the interfaced region, as shown in Supplementary Figure 1. By assuming that the spin–orbit gap at $\bar{K}$ remains unchanged, the binding energy of the K-lVBM above E_F can be extracted as the Schottky barrier height of ∼ −30 meV.

The corresponding Fermi surface of this hybrid system is shown in Figure 2f. The bands centered at $\bar{K}$ derive from the shallower binding energy branch of the spin–orbit split valleys in monolayer WSe_2, and the diffuse spectral weight at $\bar{\Gamma}$ originates from the spectral tail of the broadened WSe_2 Γ-lVBM. There are also larger features with low spectral weight centered at both the $\bar{\Gamma}$ and $\bar{M}$ points, which we attribute as signals directly from the substrate.[16,17] We note that due to the surface sensitivity of ARPES necessitating unimpeded access to sample regions of interest, characterizing the electronic structure of a semimetallic phase of WSe_2 without interfacing to $NbSe_2$ would require levels of electrostatic doping beyond that possible either with, e.g., alkali metal deposition[19] or through back gating exfoliated TMD flakes.[20]

Orbital-Dependent Localization within WSe_2/$NbSe_2$ Heterostructures

In Figure 3, the contrasting dimensionalities of in- and out-of-plane orbital-derived bands (and therefore between the $\bar{K}$ and $\bar{\Gamma}$ lVBM, respectively) are explored through photon energy-dependent ARPES, which simultaneously varies both the probed k_z plane and the electron mean free path.[21] $\bar{K}$–$\bar{\Gamma}$–$\bar{K}$ band dispersions and Fermi surface maps for 121 and 150 eV photons, shown in Figure 3a,e and 3b,f, respectively, show increased spectral weight of bands imaged directly from the $NbSe_2$ substrate relative to the datasets in Figure 2 ($h\nu$ = 91.5 eV) due to the increased effective transparency of the WSe_2 top layer. The larger electron mean free path enables both direct confirmation of the preserved underlying $NbSe_2$ band structure and clear visualization of a 24° relative twist angle between the substrate and the WSe_2 top layer. An equivalent Fermi surface from a freshly cleaved $NbSe_2$ crystal is presented in Supplementary Figure 2(a) for comparison.

While the twist angle between the monolayer and bulk components of our heterostructures is large, we do not expect it to be consequential for charge transfer between these materials. As the orbitals with a non-negligible spatial extent into the van der Waals gap contribute bands primarily to the $\bar{\Gamma}$ point in both WSe_2 and $NbSe_2$, interlayer coupling and band hybridization across the interface should be largely unhindered. Equivalently, the relevant hopping channels are available independently of twist angle.

The scale of this hybridization is shown in Figure 3d, where the k_z dependence of bands at the $\bar{\Gamma}$ point is shown. There are four features within this energy window labeled from low to high binding energy: The shallowest band closest to the Fermi level (#1 in Figure 3d) is the lVBM of WSe_2, which, as shown in Figures 2 and 3a,b, becomes significantly altered relative to the equivalent band in the free-standing case (Figure 1a and

https://doi.org/10.1021/acsnano.5c22009
ACS Nano 2026, 20, 7898–7907

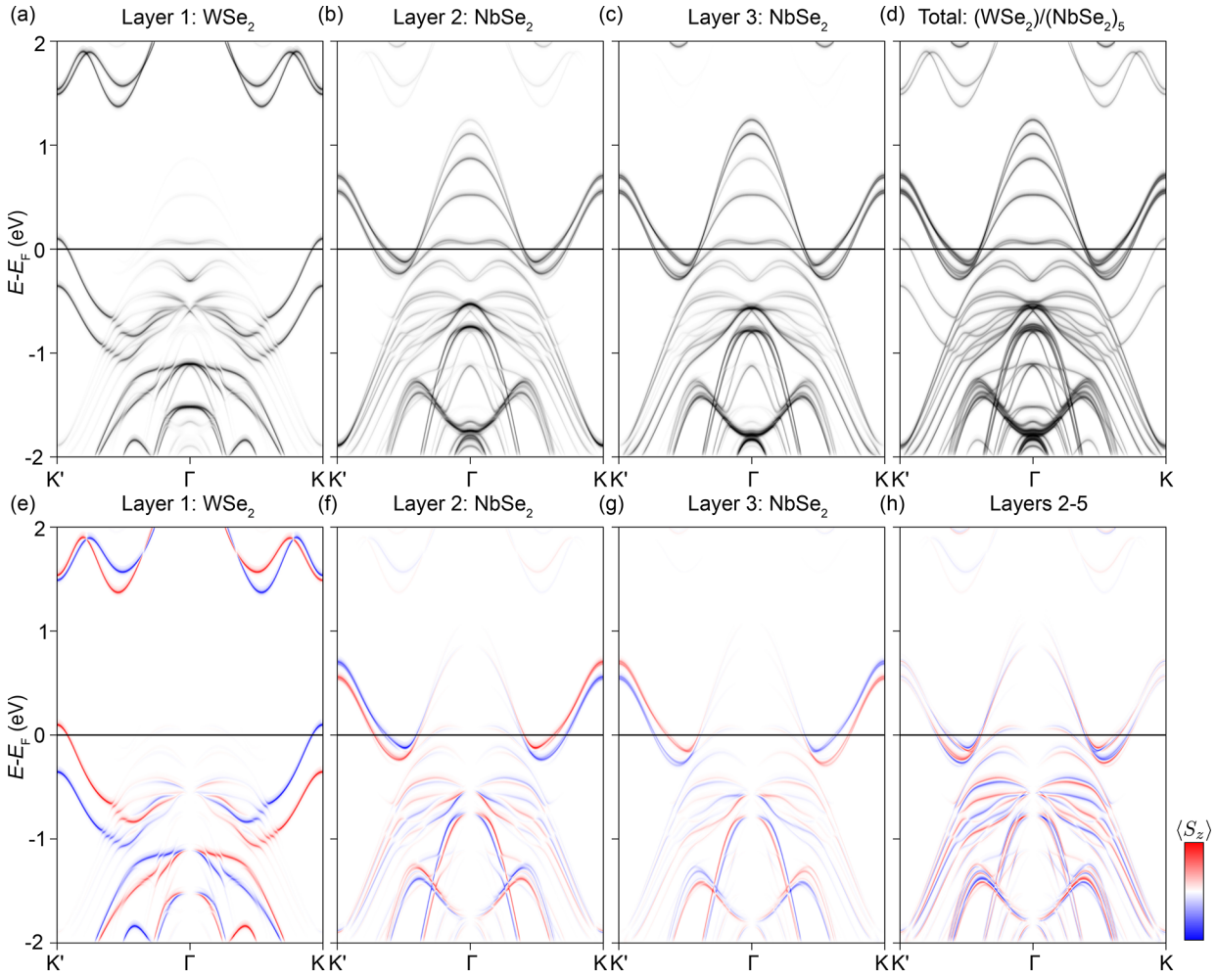

Figure 4. First-principles band structure calculations of a $(WSe_2)/(NbSe_2)_5$ heterostructure with a zero twist angle: (a−c) Layer-projected spectral function calculations to the first (a), second (b), and third (c) layers of this finite-size heterostructure. (d) Total layer-integrated spectral function calculation. (e−g) Corresponding $\langle S_z \rangle$ spin projections for the spectral functions shown in (a−c). (h) $\langle S_z \rangle$ contribution from the four $NbSe_2$ layers closest to the surface (layers 2−5).

2c). Its dispersive nature (most clearly resolved in the high k_z regime) directly evidences a delocalization along the *c*-axis into the bulk, thus permitting momentum dependence in the out-of-plane k_z direction. The other three bands are two-dimensional: the deepest bands at approximately −1.4 and −1.7 eV (#3 and #4 in Figure 3d) are mixed character Se p_{xy}- and W $d_{xz,yz}$-derived bands, which are unaffected by the details of the substrate due to the negligible *c*-axis hopping from in-plane orbitals.[8,15,22] The remaining band is a sharp 2D state at −0.9 eV without a clear analogue in the noninteracting limit. While this band could be mistaken for a second k_z sub-band within the d_{z^2} manifold present within bilayer WSe_2, its two-dimensionality relative to the lower-energy band (#1) and the unambiguous photoluminescence signal from ML WSe_2 before assembly (Figure 1c) mean that this is unlikely. Instead, we attribute this to be a signature of the bulk Dirac point and topological surface state pairs predicted in bulk 2H−$NbSe_2$.[22] Indeed, a Dirac-like band crossing is prominent in the data on bare bulk $NbSe_2$ shown in Figure 1b and Supplementary Figure 2b,c, at the same binding energy and momentum.

Figure 3c shows an equivalent k_z dispersion for the $\bar{K}$ point: in contrast to the $\bar{\Gamma}$-lVBM, the pair of spin−orbit split bands at $\bar{K}$ remain sharp, two-dimensional, and therefore monolayer-like as a function of k_z, in line with previous discussions and the W $d_{xy,\, x^2-y^2}$ orbitals from which they derive. The contrasting dimensionalities of the lVBM are further seen in the $k_y - k_z$ Fermi contour shown in Figure 3g, where bands near $\bar{\Gamma}$ and $\bar{K}$ are diffuse and well-defined, respectively. Note also that there is no evidence of band hybridization of the overlapping WSe_2 and $NbSe_2$ bands away from $\bar{\Gamma}$ in the Fermi surfaces shown in Figure 3e,f, consistent with their in-plane orbital makeup and therefore their layer-locked localization. It follows that the spin structure of the observed K-point Fermi crossings should be identical to the equivalent bands of free-standing WSe_2 monolayers, i.e., strongly spin-polarized along the out-of-plane direction.

In Figure 4, the experimentally observed orbital-dependent localization is further explored through comparisons to layer- and spin-resolved ($\langle S_z \rangle$) density functional theory-based calculations for a 1 ML-WSe_2/5 ML-$NbSe_2$ heterostructure with a zero twist angle. Despite the finite thickness of the $NbSe_2$ component and the absence of a finite twist angle, the key physics of the experimental system is extremely well captured. The shallower binding-energy K point valleys of the WSe_2 top layer cross the Fermi level to form a spin-polarized lVBM at ∼ −100 meV binding energy, reproducing the negative Schottky barrier seen experimentally. As demon-

https://doi.org/10.1021/acsnano.5c22009
ACS Nano 2026, 20, 7898−7907

strated by their layer-resolved spectral weight, these strongly spin-polarized Fermi crossings are entirely absent away from the topmost layer, in line with the above discussions.

The contrasting behavior of the $\bar{\Gamma}$-lVBM is also well-reproduced: as observed within the experimental band dispersions in Figures 2d and 3a,b,d, the Γ-lVBM of WSe_2 becomes resonant with the equivalent bands in $NbSe_2$ and is therefore delocalized through the heterostructure. The spectral weight of the collective d_{z^2} manifold at $\bar{\Gamma}$ is most prominent away from the surface (Figure 4b,c), with only very faint signatures in the WSe_2 top layer. The surface transport channels from this hybrid system should therefore be dominated by bands at $\bar{K}$ and will therefore be almost entirely spin-polarized.

We note that, while each individual $NbSe_2$ layer also carries a significant, layer-localized spin polarization at $\bar{K}$,[17] the net spin polarization from centrosymmetric 2H−$NbSe_2$ is zero due to the oppositely oriented electric dipoles between adjacent $NbSe_2$ layers. This is shown in Figure 4h, where the total $\langle S_z \rangle$ contribution from the four $NbSe_2$ layers closest to the surface is significantly reduced relative to that of an individual layer. The bulk transport properties, therefore, will be dominated by spin-degenerate carriers from large hole bands at both $\bar{\Gamma}$ and $\bar{K}$ for layer 2+, with the heavily doped surface WSe_2 monolayer being the only net contributor to the overall spin structure.

We stress that the strong agreement to the band structure calculations in Figure 4, despite the large experimental twist angle, is again strongly suggestive that both the degree of charge transfer and the resulting electronic structure are largely insensitive to the extent of the lattice mismatch between WSe_2 and $NbSe_2$, and therefore, the physics on show here can be exploited without complex assembly. This is consistent with the conclusion that interactions between out-of-plane orbital-derived states at $\bar{\Gamma}$ are primarily responsible for facilitating charge transfer. However, we do not rule out smaller twist angle dependencies: While the Schottky barrier is negative in both theory and experiment, more direct Nb−W interlayer hopping pathways may slightly enhance charge transfer. Moreover, band hybridizations driven by Moiré periodicities may become apparent for specific twist angle regimes, as was found in numerous lattice-mismatched 2H-TMD bilayers.[23,24]

Taken together, the experimental and theoretical findings in Figures 3 and 4 evidence that the states at $\bar{K}$ remain localized to the WSe_2 top layer and can therefore be considered surface states of the hybrid bulk system. There has been significant effort in characterizing materials with large atomic spin−orbit coupling which are capable of hosting Rashba-split states either at the surface (due to the surface potential step) or within the bulk (due to noncentrosymmetric crystal structures) with a large band separation.[25−31] The surface states of ML-WSe_2/$NbSe_2$ can be considered a particularly extreme example of this, with up and down spin species separated by the K−K′ separation of the BZ ($\frac{4\pi}{3a} \approx 1.3$ Å^{-1}). The momentum separation of these states should provide significant resilience against interband scattering, similar to that found in metallic surface states of topological insulators (TIs).[32]

Tunability through Thickness Augmentation

To finalize, we demonstrate how the broader physics of 2H−WSe_2 is maintained despite the significant charge doping. The $\bar{\Gamma}$ lVBM in free-standing WSe_2 forms a dispersive band continuum along k_z in the bulk limit due to non-negligible out-of-plane hopping of the d_{z^2} orbitals from which it derives. For intermediate thicknesses, it forms an array of energetically separated, doubly degenerate k_z subbands, the number of which matches the total thickness in monolayers. Since the details of the K point lVBM are relatively unaffected by the surrounding layers, the $\bar{\Gamma}$-lVBM becomes the global valence band maximum for 3+ ML.[10−14] In Figure 5, we show how this

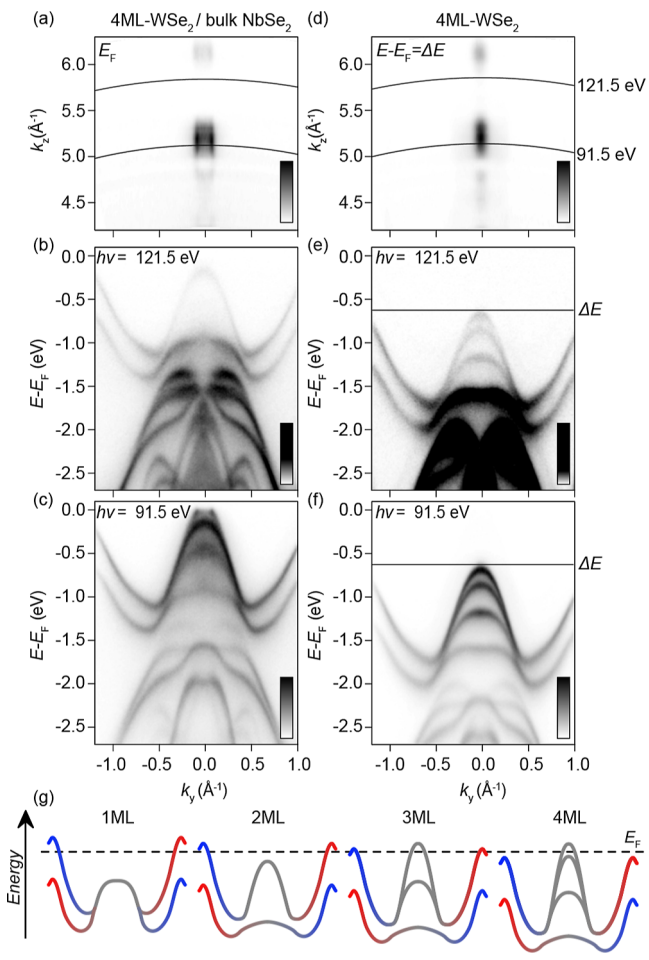

Figure 5. Singular Fermi surface in 4 ML-WSe_2/bulk $NbSe_2$: (a) Fermi level $k_y - k_z$ contour showing the dimensionality of the Fermi pocket at Γ. Black lines indicate the positioning of band dispersions presented in (b,c). (b,c) Band dispersions close to the K−Γ−K axis, taken with 121.5 (b) and 91.5 eV (c) photons. (d−f) Equivalent data sets for 4 ML-WSe_2/gr. The $k_y - k_z$ contour in (d) is presented for $E - E_F = \Delta E$, the calculated charge transfer when interfaced with bulk $NbSe_2$. (g) Schematic illustrating the likely Fermi level placement in the surface layers for 1−4 ML-WSe_2/bulk $NbSe_2$.

c-axis delocalization of out-of-plane orbital-derived electrons within the WSe_2 top layers drastically alters the Fermiology of interfaced systems. In Figure 5a−f, ARPES spectra from 4 ML-WSe_2, where the global valence band maximum is at the Γ point,[33−35] and a 4 ML-WSe_2/bulk $NbSe_2$ system are compared. In analogy to the monolayer scenario, the charge transfer acts to shift the WSe_2 bands toward the Fermi level by $\Delta E \approx 0.63$ eV, as calculated from the shift of the 2D state at Γ and ∼ −2.2 eV in pristine 4 ML-WSe_2. With this, the global VBM of 4 ML-WSe_2 at $\bar{\Gamma}$ creates a singular Fermi surface. As the four quantized bands at $\bar{\Gamma}$ sample the continuous k_z-dispersive global VBM of bulk WSe_2, the Fermi pocket is not visible for all photon energies, instead exhibiting periodic spectral weight in k_z (Figure 5a,d)). The valence band top is

https://doi.org/10.1021/acsnano.5c22009
ACS Nano 2026, 20, 7898−7907

therefore visible and absent for 91.5 and 121.5 eV photons, respectively, as shown in Figure 5b,c. We note that the spacing and appearance of the four discrete W d_{z^2} subbands at $\bar{\Gamma}$ are slightly altered relative to free-standing 4 ML-WSe_2 (Figure 5d–f), again likely due to interactions with the out-of-plane Nb d and Se p orbital-derived bands of the bulk substrate.

The 0.63 eV energy shift of the bands in the 4 ML scenario is smaller than observed for the monolayer limit (~0.85 eV), but the resulting Luttinger count is similar (~10^{13} cm^{-2} in both cases when assuming that Fermi surfaces formed in the ML and 4 ML scenarios have degeneracies of 1 and 2, respectively[36]). The reduced potential difference and constant carrier density are consistent with the increased thickness of the WSe_2 top layer and therefore the increased separation of displaced charge.

As schematized in Figure 5g, one should expect that the 2 and 3 ML scenarios produce the intermediate scenarios: the gradual shift of the global VBM from K to Γ with increasing film thickness should result in distinct Fermi surfaces from those observed in our systems, and there may exist a thickness where both Fermi surfaces exist simultaneously. A similar $\bar{\Gamma}$-centered Fermiology was achieved recently by interfacing few-layer WSe_2 with few-layer $NbSe_2$,[37] demonstrating how similar behavior can be achieved without a bulk component (evidenced also through the calculations for finite-thickness $NbSe_2$ in Figure 4), increasing suitability for integration into devices. We note, however, that pairing WSe_2 to few-layer $NbSe_2$ will generically result in the generation of well-defined and delocalized states within the array of d_{z^2} derived bands at $\bar{\Gamma}$, in addition to those schematized in Figure 5g, potentially polluting surface transport signals from K/K′.[37]

CONCLUSIONS

In conclusion, we have demonstrated that matching thin flakes of WSe_2 to many-layer $NbSe_2$ single crystals creates p-type contacts with negative Schottky barriers, and the momenta and spin degeneracy of the charge carriers at the interface can be tuned with the thickness of the WSe_2 overlay.

For the case of monolayer WSe_2, the Fermi level is shifted between the local band maximum at Γ and the global valence band maximum at K. While the band at Γ becomes resonant with out-of-plane orbitals from $NbSe_2$ and hence delocalized into the bulk, the K′ and K point valleys remain localized to the WSe_2 monolayer due to their in-plane orbital makeup. This observed localization alongside our density functional theory calculations together implies that the spin-valley locking of free-standing WSe_2 monolayers is preserved. The hybrid $WSe_2/NbSe_2$ system thus behaves analogously to a bulk solid wherein Rashba-split surface states cross the Fermi level, but with out-of-plane spin polarization and a maximized momentum separation.

The semimetallic equilibrium state found here is likely further tunable through gating, and the relative size of the spin-polarized hole pockets at K and K′ could be potentially changed with, e.g., uniaxial strain or applied electric fields. It is noteworthy that 2H–$NbSe_2$ possesses competing charge density wave (CDW) and superconducting phases, which are strongly thickness dependent (transition temperatures of ~34 and 7 K, respectively, in the bulk limit).[38−41] While the twist angle between the WSe_2 monolayer and bulk $NbSe_2$ is large in this proof-of-principle example, other twist angles could lead to a pronounced Moiré periodicity, which could be sensitive to the CDW reconstruction of the substrate.[42] More excitingly, the superconducting phases of $NbSe_2$ could lead to odd-parity pairing between the spin-polarized Fermi pockets, a scenario which is thought to be one pathway toward topological superconductivity.[43] More generally, this work bolsters the collective electronic properties of interfaced TMD systems[23,24,37,44−47] while providing spectroscopic evidence for electronically ohmic contacts with negative Schottky barriers between a TMD semiconductor and metal, a result of technological importance for the ultimate optimization and miniaturization of electronic devices.

METHODS/EXPERIMENTAL SECTION

Heterostructure Fabrication

The photoemission spectra from bulk $NbSe_2$ in Figure 1b and Supplementary Figure 2 originate from high-quality single crystals of $NbSe_2$, cleaved *in situ* in measurement conditions with a standard top post method. All TMD flakes were exfoliated onto polydimethylsiloxane (PDMS) using blue tape, and their thicknesses were verified through photoluminescence spectroscopy (e.g., Figure 1d, performed with a diode-pumped solid-state CW 532 nm laser, focused with a 100× objective on the flake of interest) and/or by comparing optical images and photoemission spectra to those of known references. The ML-WSe_2/bulk $NbSe_2$ heterostructure characterized in Figures 2 and 3 and Supplementary Figure 1 is created through the transfer of a monolayer WSe_2 from PDMS to a freshly cleaved bulk $NbSe_2$ crystal in an Ar atmosphere. The sample is then rinsed with diisopropylamine, isopropanol, and ethanol and annealed in UHV at 200 °C for 3 + h prior to photoemission experiments. For the 4 ML-WSe_2/bulk $NbSe_2$ sample in Figure 5, a many-layer flake of $NbSe_2$ was transferred from PDMS onto a graphite/*n*-type Si substrate within an Ar glovebox. Following chemical rinsing and annealing, the 4 ML region of WSe_2 was then transferred on top. The sample is then rinsed again and annealed in UHV at 200 °C for 3+ hours prior to photoemission experiments. The 'free-standing' flakes of WSe_2 shown in Figures 1, 2, and 5 were prepared in one of two different ways: the 1 and 4 ML WSe_2 flakes in Figure 1a and Figure 5d–f, respectively, were transferred in air from PDMS onto graphite/*n*-type Si substrates. After a chemical rinse, the samples were annealed in UHV at 270 °C for 3 + h prior to photoemission. The role of the graphite is to prevent the WSe_2 flake from being lost during the chemical rinsing process. The ML flake in Figure 2c was transferred in air onto a *h*BN/undoped Si substrate and grounded via graphene to Au contacts. The sample was chemically rinsed and annealed in a constant-flow Ar furnace at 100 °C for 1 h after each stacking stage and annealed in UHV at 270 °C prior to photoemission.

Photoemission

Photoemission data were acquired from one of three sources: (1) A nano-ESCA system with a helium lamp (NanoESCA III at FMMA (ROR: 04z91ja70)[48]) at room temperature was used for the spectra in Figure 1a. (2) Nanofocused angle-resolved photoemission (nano-ARPES) (~2 μm light spot) at the MAESTRO beamline of the Advanced Light Source (LBNL) was used for the data in Figures 2 and 5 and Supplementary Figure 1, acquired at cryogenic temperatures of ~25 K with *p*-polarized photons of energies between 60 and 150 eV. (3) The i05 beamline of Diamond Light Source was utilized for the data in Figure 1b and Supplementary Figure 2, acquired at ~10 K with *p*-polarized photons of between 106 and 121 eV. Mapping from photon energy to k_z was done using the free-electron final state assumption,[21] assuming an inner potential of 13 eV to match that found for bulk WSe_2.[8]

Theory

Electronic structure calculations were performed within density functional theory using the Perdew–Burke–Ernzerhof exchange–correlation functional,[49] as implemented in the Quantum ESPRESSO package.[50,51] We used the norm-conserving pseudopotentials[52] and plane-wave basis set with a cutoff energy of 70 Ry. Due to the close

https://doi.org/10.1021/acsnano.5c22009
ACS Nano 2026, 20, 7898−7907

similarity between the lattice parameters of 2H−WSe_2 and 2H−$NbSe_2$, the experimentally reported bulk structure of 2H−WSe_2[53] was used for both compounds in constructing WSe_2/$NbSe_2$ heterostructures. A unit cell containing 1 ML WSe_2 and five-layer $NbSe_2$ with a zero twist angle was employed, with a vacuum spacing of 40 Å to prevent spurious interactions between periodic images. The Brillouin zone was sampled using a k−point mesh of 12 × 12 × 1. Spin and orbital projections were obtained using Wannier functions,[54,55] downfolded from the DFT Hamiltonian, with the valence d orbitals of the transition−metal atoms and the Se 4p orbitals chosen as projection centers.

■ ASSOCIATED CONTENT

Data Availability Statement

Data are available from the authors upon reasonable request.

Supporting Information

The Supporting Information is available free of charge at https://pubs.acs.org/doi/10.1021/acsnano.5c22009.

Supplemental data sets demonstrating homogeneity of the 1 ML-WSe_2/$NbSe_2$ interface and reference data for bulk $NbSe_2$ (PDF)

■ AUTHOR INFORMATION

Corresponding Author

Oliver J. Clark − *School of Physics and Astronomy, Monash University, Clayton, Victoria 3168, Australia; Diamond Light Source, Harwell Science and Innovation Campus, Didcot OX11 0DE, U.K.;* orcid.org/0000-0002-3092-9465; Email: oliver.clark@diamond.ac.uk

Authors

Anugrah Azhar − *Department of Physics and Astronomy, University of Manchester, Manchester M13 9PL, U.K.; Physics Study Program, Faculty of Science and Technology, Syarif Hidayatullah State Islamic University Jakarta, Tangerang Selatan 15412, Indonesia*

Thi-Hai-Yen Vu − *School of Physics and Astronomy, Monash University, Clayton, Victoria 3168, Australia*

Benjamin A. Chambers − *Flinders Microscopy and Microanalysis, Flinders University, Adelaide, South Australia 5042, Australia;* orcid.org/0000-0001-5026-4635

Federico Mazzola − *Department of Physics and Astronomy 'Galileo Galilei', University of Padova, Padova, Italy; CNR-SPIN UOS Napoli, Complesso Universitario di Monte Sant'Angelo, 80126 Napoli, Italy*

Sadhana Sridhar − *School of Physics and Astronomy, Monash University, Clayton, Victoria 3168, Australia*

Geetha Balakrishnan − *Department of Physics, University of Warwick, Coventry CV4 7AL, U.K.*

Aaron Bostwick − *Advanced Light Source, Lawrence Berkeley National Laboratory, Berkeley, California 94720, United States*

Chris Jozwiak − *Advanced Light Source, Lawrence Berkeley National Laboratory, Berkeley, California 94720, United States;* orcid.org/0000-0002-0980-3753

Eli Rotenberg − *Advanced Light Source, Lawrence Berkeley National Laboratory, Berkeley, California 94720, United States;* orcid.org/0000-0002-3979-8844

Sarah L. Harmer − *Institute for Nanoscale Science and Technology and Flinders Microscopy and Microanalysis, Flinders University, Adelaide, South Australia 5042, Australia*

Mohammad Saeed Bahramy − *Department of Physics and Astronomy, University of Manchester, Manchester M13 9PL, U.K.*

Michael S. Fuhrer − *School of Physics and Astronomy and ARC Centre for Future Low Energy Electronics Technologies, Monash University, Clayton, Victoria 3168, Australia;* orcid.org/0000-0001-6183-2773

Mark T. Edmonds − *School of Physics and Astronomy and ARC Centre for Future Low Energy Electronics Technologies, Monash University, Clayton, Victoria 3168, Australia; Melbourne Centre for Nanofabrication, Victorian Node of the Australian National Fabrication Facility, ANFF-VIC Technology Fellow, Clayton, Victoria 3168, Australia;* orcid.org/0000-0001-8054-5470

Complete contact information is available at: https://pubs.acs.org/10.1021/acsnano.5c22009

Author Contributions

O.J.C. constructed the WSe_2/$NbSe_2$ heterostructures. G.B. grew the $NbSe_2$ single crystals. O.J.C., T.-H.-Y.V., F.M., and S.S. performed photoemission measurements, supported by A.B., C.J., and E.R. O.J.C. and B.A.C. performed the nano-ESCA measurements. A.A. and M.S.B. performed the density functional theory-based calculations. O.J.C. performed the photoluminescence measurements. B.A.C. and S.L.H. provided access to the nano-ESCA instrument at Flinders University, South Australia. O.J.C. wrote the manuscript with significant contributions from M.S.F. and M.T.E. and further contributions from all other authors. O.J.C. was responsible for project planning and direction.

Notes

The authors declare no competing financial interest.

■ ACKNOWLEDGMENTS

O.J.C., M.S.F., and M.T.E. acknowledge funding support from ARC Discovery Project DP200101345. M.T.E. acknowledges funding support from ARC Future Fellowship FT220100290. O.J.C. acknowledges travel funding provided by the International Synchrotron Access Program (ISAP) managed by the Australian Synchrotron, part of ANSTO, and funded by the Australian Government. G.B. gratefully acknowledges EPSRC, UK for funding through Grant EP/T005963/1. A.A. and M.S.B. gratefully acknowledge the Research Infrastructures at the Center for Computational Materials Science at the Institute for Materials Research for allocations on the MASAMUNE-IMR supercomputer system (Project No. 202112-SCKXX-0510) and the MAHAMERU BRIN HPC facility under the National Research and Innovation Agency of Indonesia. M.S.B. acknowledges support from the Leverhulme Trust (Grant No. RPG-2023-253). A.A. had support from the Indonesia Endowment Fund for Education (LPDP), NIB/202209223311735. This research used resources of the Advanced Light Source, which is a DOE Office of Science User Facility under contract no. DE-AC02-05CH11231. This work was performed in part at the Melbourne Centre for Nanofabrication (MCN) in the Victorian Node of the Australian National Fabrication Facility (ANFF). The authors acknowledge the facilities and the scientific and technical assistance of Microscopy Australia (ROR: 042mm0k03) enabled by NCRIS and the government of South Australia at Flinders Microscopy and Microanalysis (ROR: 04z91ja70), Flinders University (ROR: 01kpzv902).

https://doi.org/10.1021/acsnano.5c22009
ACS Nano 2026, 20, 7898−7907

REFERENCES

(1) Patoary, N. H.; Xie, J.; Zhou, G.; Al Mamun, F.; Sayyad, M.; Tongay, S.; Esqueda, I. S. Improvements in 2D p-Type WSe_2 Transistors Towards Ultimate CMOS Scaling. *Sci. Rep.* **2023**, *13*, 3304.

(2) Park, H.; Shin, H.; Ali, N.; Choi, H.; Kim, B. S. Y.; Kang, B.; Choi, M. S.; Yoo, W. J. P-Type Vertical FETS Realized by Using Fermi-level Pinning-Free 2D Metallic Electrodes. *Nano Lett.* **2025**, *25*, 368.

(3) Sata, Y.; Moriya, R.; Masubuchi, S.; Watanabe, K.; Taniguchi, T.; Machida, T. N- and p-Type Carrier Injections into WSe_2 with van der Waals Contacts of Two-Dimensional Materials. *Jpn. J. Appl. Phys.* **2017**, *56*, 04CK09.

(4) Hu, H.; Wang, Z.; Pan, M.; Chen, Y.; Han, Y.; Wang, J. Interface Effects in Metal-2D TMDs Systems: Advancing the Design and Development Electrocatalysts. *Adv. Sci.* **2025**, *12*, 2500226.

(5) Xiao, D.; Liu, G.-B.; Feng, W.; Xu, X.; Yao, W. Coupled Spin and Valley Physics in Monolayers of MoS_2 and Other Group-VI Dichalcogenides. *Phys. Rev. Lett.* **2012**, *108*, 196802.

(6) Zeng, H.; Dai, J.; Yao, W.; Xiao, D.; Cui, X. Valley Polarization in MoS_2 monolayers by Optical Pumping. *Nat. Nanotechnol.* **2012**, *7*, 490.

(7) Mak, K. F.; He, K.; Shan, J.; Heinz, T. F. Control of Valley Polarization in Monolayer MoS_2 by Optical Helicity. *Nat. Nanotechnol.* **2012**, *7*, 494.

(8) Riley, J. M.; Mazzola, F.; Dendzik, M.; Michiardi, M.; Takayama, T.; Bawden, L.; Granerød, C.; Leandersson, M.; Balasubramanian, T.; Hoesch, M.; Kim, T. K.; Takagi, H.; Meevasana, W.; Hofmann, P.; Bahramy, M. S.; Wells, J. W.; King, P. D. C. Direct Observation of Spin-Polarized Bulk Bands in an Inversion-Symmetric Semiconductor. *Nat. Phys.* **2014**, *10*, 835.

(9) Yuan, H.; Bahramy, M. S.; Morimoto, K.; Wu, S.; Nomura, K.; Yang, B.-J.; Shimotani, H.; Suzuki, R.; Toh, M.; Kloc, C.; Xu, X.; Arita, R.; Nagaosa, N.; Iwasa, Y. Zeeman-Type Spin Splitting Controlled by an Electric Field. *Nat. Phys.* **2013**, *9*, 563.

(10) Latzke, D. W.; Zhang, W.; Suslu, A.; Chang, T.-R.; Lin, H.; Jeng, H.-T.; Tongay, S.; Wu, J.; Bansil, A.; Lanzara, A. Electronic Structure, Spin-Orbit Coupling, and Interlayer Interaction in Bulk MoS_2 and WS_2. *Phys. Rev. B* **2015**, *91*, 235202.

(11) Kim, B. S.; Rhim, J.-W.; Kim, B.; Kim, C.; Park, S. R. Determination of the Band Parameters of Bulk 2H-MX_2 (M = Mo, W; X = S, Se) by Angle-Resolved Photoemission Spectroscopy. *Sci. Rep.* **2016**, *6*, 36389.

(12) Alarab, F.; Minar, J.; Constantinou, P.; Nafday, D.; Schmitt, T.; Wang, X.; Strocov, V. N. k-Dependent Proximity-Induced Modulation of Spin-Orbit Interaction in $MoSe_2$ Interfaced with Amorphous Pb. *Nat. Commun.* **2025**, *17*, 1076.

(13) Salazar, R.; Jamet, M.; Vergnaud, C.; Pulkkinen, A.; Bertran, F.; Bigi, C.; Minár, J.; Ouerghi, A.; Jaouen, T.; Rault, J.; Le Fèvre, P. Two-Dimensional to Bulk Crossover of the WSe_2 Electronic Band Structure. *Electron. Struct.* **2025**, *7*, 025008.

(14) Chang, T.-R.; Lin, H.; Jeng, H.-T.; Bansil, A. Thickness Dependence of Spin Polarization and Electronic Structure of Ultra-Thin Films of MoS_2 and Related Transition-Metal Dichalcogenides. *Sci. Rep.* **2014**, *4*, 6270.

(15) Chhowalla, M.; Shin, H. S.; Eda, G.; Li, L.-J.; Loh, K. P.; Zhang, H. The Chemistry of Two-Dimensional Layered Transition Metal Dichalcogenide Nanosheets. *Nat. Chem.* **2013**, *5*, 263.

(16) Borisenko, S. V.; Kordyuk, A. A.; Zabolotnyy, V. B.; Inosov, D. S.; Evtushinsky, D.; Büchner, B.; Yaresko, A. N.; Varykhalov, A.; Follath, R.; Eberhardt, W.; Patthey, L.; Berger, H. Two Energy Gaps and Fermi-Surface "Arcs" in $NbSe_2$. *Phys. Rev. Lett.* **2009**, *102*, 166402.

(17) Bawden, L.; Cooil, S. P.; Mazzola, F.; Riley, J. M.; Collins-McIntyre, L. J.; Sunko, V.; Hunvik, K. W. B.; Leandersson, M.; Polley, C. M.; Balasubramanian, T.; Kim, T. K.; Hoesch, M.; Wells, J. W.; Balakrishnan, G.; Bahramy, M. S.; King, P. D. C. Spin–Valley Locking in the Normal State of a Transition-Metal Dichalcogenide Superconductor. *Nat. Commun.* **2016**, *7*, 11711.

(18) Tonndorf, P.; Schmidt, R.; Böttger, P.; Zhang, X.; Börner, J.; Liebig, A.; Albrecht, M.; Kloc, C.; Gordan, O.; Zahn, D. R. T.; Michaelis de Vasconcellos, S.; Bratschitsch, R. Photoluminescence Emission and Raman Response of Monolayer MoS_2, $MoSe_2$, and WSe_2. *Opt. Express* **2013**, *21*, 4908.

(19) Riley, J. M.; Meevasana, W.; Bawden, L.; Asakawa, M.; Takayama, T.; Eknapakul, T.; Kim, T. K.; Hoesch, M.; Mo, S. K.; Takagi, H.; Sasagawa, T.; Bahramy, M. S.; King, P. D. C. Negative Electronic Compressibility and Tunable Spin Splitting in WSe_2. *Nat. Nanotechnol.* **2015**, *10*, 1043.

(20) Nguyen, P. V.; Teutsch, N. C.; Wilson, N. P.; Kahn, J.; Xia, X.; Graham, A. J.; Kandyba, V.; Giampietri, A.; Barinov, A.; Constantinescu, G. C.; Yeung, N.; Hine, N. D. M.; Xu, X.; Cobden, D. H.; Wilson, N. R. Visualizing Electrostatic Gating Effects in Two-Dimensional Heterostructures. *Nat.* **2019**, *572*, 220.

(21) Damascelli, A. Probing the Electronic Structure of Complex Systems by ARPES. *Phys. Scr.* **2004**, *T109*, 61.

(22) Bahramy, M. S.; Clark, O. J.; Yang, B.-J.; Feng, J.; Bawden, L.; Riley, J. M.; Marković, I.; Mazzola, F.; Sunko, V.; Biswas, D.; Cooil, S. P.; Jorge, M.; Wells, J. W.; Leandersson, M.; Balasubramanian, T.; Fujii, J.; Vobornik, I.; Rault, J.; Kim, T. K.; Hoesch, M.; Okawa, K.; et al. Ubiquitous Formation of Bulk Dirac Cones and Topological Surface States from a Single Orbital Manifold in Transition-Metal Dichalcogenides. *Nat. Mater.* **2018**, *17*, 21–28.

(23) Devakul, T.; Crépel, V.; Zhang, Y.; Fu, L. Magic in Twisted Transition Metal Dichalcogenide Bilayers. *Nat. Commun.* **2021**, *12*, 6730.

(24) Guo, Y.; Pack, J.; Swann, J.; Holtzman, L.; Cothrine, M.; Watanabe, K.; Taniguchi, T.; Mandrus, D.; Barmak, K.; Hone, J.; Millis, A. J.; Pasupathy, A. N.; Dean, C. R. Superconductivity in 5.0° Twisted Bilayer WSe_2. *Nat.* **2025**, *637*, 839–845.

(25) Zhai, Y.; Baniya, S.; Zhang, C.; Li, J.; Haney, P.; Sheng, C.-X.; Ehrenfreund, E.; Vardeny, Z. V. Giant Rashba Splitting in 2D Organic-Inorganic Halide Perovskites Measured by Transient Spectroscopies. *Sci. Adv.* **2017**, *3*, No. e1700704.

(26) Sunko, V.; Rosner, H.; Kushwaha, P.; Khim, S.; Mazzola, F.; Bawden, L.; Clark, O. J.; Riley, J. M.; Kasinathan, D.; Haverkort, M. W.; Kim, T. K.; Hoesch, M.; Fujii, J.; Vobornik, I.; Mackenzie, A. P.; King, P. D. C. Maximal Rashba-Like Spin Splitting via Kinetic-Energy-Coupled Inversion-Symmetry Breaking. *Nat.* **2017**, *549*, 492.

(27) Ishizaka, K.; Bahramy, M. S.; Murakawa, H.; Sakano, M.; Shimojima, T.; Sonobe, T.; Koizumi, K.; Shin, S.; Miyahara, H.; Kimura, A.; Miyamoto, K.; Okuda, T.; Namatame, H.; Taniguchi, M.; Arita, R.; Nagaosa, N.; Kobayashi, K.; Murakami, Y.; Kumai, R.; Kaneko, Y.; et al. Giant Rashba-Type Spin Splitting in Bulk BiTeI. *Nat. Mater.* **2011**, *10*, 521.

(28) Bian, G.; Wang, X.; Millar, T.; Chiang, T.-C. Origin of giant Rashba spin splitting in Bi/Ag surface alloys. *Phys. Rev. B* **2013**, *88*, 085427.

(29) Bianchi, M.; Hatch, R. C.; Li, Z.; Hofmann, P.; Song, F.; Mi, J.; Iversen, B. B.; Abd El-Fattah, Z. M.; Löptien, P.; Zhou, L.; Khajetoorians, A. A.; Wiebe, J.; Wiesendanger, R.; Wells, J. W. Robust Surface Doping of Bi_2Se_3 by Rubidium Intercalation. *ACS Nano* **2012**, *6*, 7009.

(30) Feng, R.; Zhang, Y.; Li, J.; Li, Q.; Bao, C.; Zhang, H.; Chen, W.; Tang, X.; Yaegashi, K.; Sugawara, K.; Sato, T.; Duan, W.; Yu, P.; Zhou, S. Giant Rashba Splitting in PtTe/$PtTe_2$ Heterostructure. *Nat. Commun.* **2025**, *16*, 2667.

(31) Picozzi, S. Ferroelectric Rashba Semiconductors as a Novel Class of Multifunctional Materials. *Front. Phys.* **2014**, *2*..

(32) Hasan, M. Z.; Kane, C. L. Colloquium: Topological Insulators. *Rev. Mod. Phys.* **2010**, *82*, 3045.

(33) Mak, K. F.; Lee, C.; Hone, J.; Shan, J.; Heinz, T. F. Atomically Thin MoS_2: A New Direct-Gap Semiconductor. *Phys. Rev. Lett.* **2010**, *105*, 136805.

(34) Sun, Y.; Wang, D.; Shuai, Z. *The Journal of Physical Chemistry C*, Indirect-to-Direct Band Gap Crossover in Few-Layer Transition Metal Dichalcogenides: A Theoretical Prediction. *J. Phys. Chem. C* **2016**, *120*, 21866.

https://doi.org/10.1021/acsnano.5c22009
ACS Nano 2026, 20, 7898–7907

(35) Ernandes, C.; Khalil, L.; Almabrouk, H.; Pierucci, D.; Zheng, B.; Avila, J.; Dudin, P.; Chaste, J.; Oehler, F.; Pala, M.; Bisti, F.; Brulé, T.; Lhuillier, E.; Pan, A.; Ouerghi, A. Indirect to Direct band Gap Crossover in Two-Dimensional $WS_{2(1-x)}Se_2x$ Alloys. *npj 2D Mater. Appl.* **2021**, *5*, 7.
(36) Luttinger, J. M.; Ward, J. C. Ground-State Energy of a Many-Fermion System. II. *Phys. Rev.* **1960**, *118*, 1417.
(37) Clark, O. J.; Azhar, A.; Chambers, B. A.; McEwen, D.; Vu, T.-H.-Y.; Bhuiyan, M. T. H.; Belosludov, R. H.; A, B.; Jozwiak, C.; Rotenberg, E.; Lee, S. H.; Mao, Z.; Balakrishnan, G.; Mazzola, F.; Harmer, S. L.; Fuhrer, M. S.; Bahramy, M. S.; Edmonds, M. T. Dimensional band engineering in asymmetrical van der Waals heterostructures. *Newton* **2026**, 100401.
(38) Xi, X.; Zhao, L.; Wang, Z.; Berger, H.; Forró, L.; Shan, J.; Mak, K. F. Strongly Enhanced Charge-Density-Wave Order in Monolayer $NbSe_2$. *Nat. Nanotechnol.* **2015**, *10*, 765.
(39) Dvir, T.; Massee, F.; Attias, L.; Khodas, M.; Aprili, M.; Quay, C. H. L.; Steinberg, H. Spectroscopy of Bulk and Few-Layer Superconducting $NbSe_2$ With van der Waals Tunnel Junctions. *Nat. Commun.* **2018**, *9*, 598.
(40) Hamill, A.; Heischmidt, B.; Sohn, E.; Shaffer, D.; Tsai, K.-T.; Zhang, X.; Xi, X.; Suslov, A.; Berger, H.; Forró, L.; Burnell, F. J.; Shan, J.; Mak, K. F.; Fernandes, R. M.; Wang, K.; Pribiag, V. S. Two-Fold Symmetric Superconductivity in Few-Layer $NbSe_2$. *Nat. Phys.* **2021**, *17*, 949.
(41) Xi, X.; Wang, Z.; Zhao, W.; Park, J.-H.; Law, K. T.; Berger, H.; Forró, L.; Shan, J.; Mak, K. F. Ising Pairing in Superconducting $NbSe_2$ Atomic Layers. *Nat. Phys.* **2016**, *12*, 139.
(42) Yoshizawa, S.; Sagisaka, K.; Sakata, H. Visualization of Alternating Triangular Domains of Charge Density Waves in 2*H*-$NbSe_2$ by Scanning Tunneling Microscopy. *Phys. Rev. Lett.* **2024**, *132*, 056401.
(43) Sato, M.; Ando, Y. Topological Superconductors: A Review. *Rep. Prog. Phys.* **2017**, *80*, 076501.
(44) Shao, Q.; Yu, G.; Lan, Y.-W.; Shi, Y.; Li, M.-Y.; Zheng, C.; Zhu, X.; Li, L.-J.; Amiri, P. K.; Wang, K. L. Strong Rashba-Edelstein Effect-Induced Spin−Orbit Torques in Monolayer Transition Metal Dichalcogenide/Ferromagnet Bilayers. *Nano Lett.* **2016**, *16*, 7514.
(45) He, S.; Yin, C.; Zhang, L.; Chen, Y.; Peng, H.; Shan, A.; Zhao, L.; Gao, L. All-2D Asymmetric Self-Powered Photodetectors with Ultra-Fast Photoresponse Based on Gr/WSe_2/$NbSe_2$ Van der Waals Heterostructure. *J. Mater. Sci. Technol.* **2025**, *219*, 205.
(46) Vu, V. T.; Nguyen, M. C.; Kim, W. K.; Do, V. D.; Dat, V. K.; Yu, W. J. Synthesis of $NbSe_2$/Bilayer Nb-Doped WSe_2 Heterostructure from Exfoliated WSe_2 Flakes. *Small Struct.* **2024**, *5*, 2300401.
(47) Fang, H.; Lin, Q.; Zhang, Y.; Thompson, J.; Xiao, S.; Sun, Z.; Malic, E.; Dash, S. P.; Wieczorek, W. Localization and Interaction of Interlayer Excitons in $MoSe_2$/WSe_2 Heterobilayers. *Nat. Commun.* **2023**, *14*, 6910.
(48) *Scienta Omicron NanoESCA III Photoemission Electron Microscope (PEEM)*. DOI: 10.25957/flinders.nanoesca3.
(49) Perdew, J. P.; Burke, K.; Ernzerhof, M. Generalized Gradient Approximation Made Simple. *Phys. Rev. Lett.* **1996**, *77*, 3865.
(50) Giannozzi, P.; Baroni, S.; Bonini, N.; Calandra, M.; Car, R.; Cavazzoni, C.; Ceresoli, D.; Chiarotti, G.; Cococcioni, M.; Dabo, I.; Dal Corso, A.; de Gironcoli, S.; Fabris, S.; Fratesi, G.; Gebauer, R.; Gerstmann, U.; Gougoussis, C.; Kokalj, A.; Lazzeri, M.; Martin-Samos, L.; et al. QUANTUM ESPRESSO: A Modular and Open-Source Software Project for Quantum Simulations of Materials. *J. Phys.:Condens. Matter* **2009**, *21*, 395502.
(51) Giannozzi, P.; Andreussi, O.; Brumme, T.; Bunau, O.; Buongiorno Nardelli, M.; Calandra, M.; Car, R.; Cavazzoni, C.; Ceresoli, D.; Cococcioni, M.; Colonna, N.; Carnimeo, I.; Dal Corso, A.; de Gironcoli, S.; Delugas, P.; DiStasio, R. A.; Ferretti, A.; Floris, A.; Fratesi, G.; Fugallo, G.; et al. Advanced Capabilities for Materials Modelling with QUANTUM ESPRESSO. *J. Phys.:Condens. Matter* **2017**, *29*, 465901.
(52) Hamann, D. R. Optimized Norm-Conserving Vanderbilt Pseudopotentials. *Phys. Rev. B* **2013**, *88*, 085117.
(53) Schutte, W.; De Boer, J.; Jellinek, F. Crystal Structures of Tungsten Disulfide and Diselenide. *J. Solid State Chem.* **1987**, *70*, 207.
(54) Mostofi, A. A.; Yates, J. R.; Lee, Y.-S.; Souza, I.; Vanderbilt, D.; Marzari, N. wannier90: A Tool For Obtaining Maximally-Localised Wannier functions. *Comput. Phys. Commun.* **2008**, *178*, 685.
(55) Souza, I.; Marzari, N.; Vanderbilt, D. Maximally Localized Wannier Functions for Entangled Energy Bands. *Phys. Rev. B* **2001**, *65*, 035109.

https://doi.org/10.1021/acsnano.5c22009
ACS Nano 2026, 20, 7898−7907